



UV Light-Induced Reversible Wettability and Sensing Performance for Ca/Mg-Doped ZnO Nanostructures via Chemical Bath Deposition

Faran Baig¹ · Ali Asif¹ · Muhammad Waseem Ashraf¹

Received: 11 February 2021 / Accepted: 17 April 2021 / Published online: 13 May 2021
© The Minerals, Metals & Materials Society 2021

Abstract

Calcium-doped zinc oxide (CaZnO) and magnesium-doped zinc oxide (MgZnO) nanostructures were synthesized by a chemical bath deposition method. X-ray diffraction results revealed c-axis plane dominance for the ZnO and MgZnO samples, and a-axis plane dominance for the CaZnO samples. Scanning electron microscopy results showed well-aligned nanorods for the ZnO and MgZnO nanostructures. However, flower- and cotton-type surface was found for the Ca-doped samples. Energy-dispersive spectroscopy results confirmed the calcium and magnesium dopants. Band gap values of 3.20 eV and 3.34 eV were revealed for higher doping concentrations of calcium and magnesium, respectively. The super-hydrophobic state was observed for the 5% Mg-doped ZnO sample, with a water contact angle of 152°. However, a hydrophobic state was observed for the 5% Ca-doped ZnO sample, with a water contact angle of 90°. The super-hydrophilic state was detected for all samples by the induction of ultraviolet light. Better contact angle reduction rates with values of 0.022 and 0.023 were estimated for the calcium-doped nanostructure. The contact angle recovery time was also evaluated, and values of 35 h and 40 h were achieved for Ca- and Mg-doped samples, respectively. The ultraviolet sensing performance was evaluated for all the samples, and the best photo-response was obtained for the 5% Mg-doped ZnO sample.

Keywords ZnO thin films · CBD · super-hydrophobic · super-hydrophilic · UV sensor

Introduction

Ultraviolet (UV) sensors play a crucial role in many applications, not only by detecting harmful UV radiation but also by enabling controlled exposure to UV radiation via regulatory control systems. These applications include and optical communication, missile plume detection and monitoring of air quality.^{1,2} The major needs for the fabrication of these sensors are high sensitivity and low-cost design.

Wettability of surfaces is another important property, which is determined by the geometry of the surface. The demand for controllable wettability is high for applications such as biological and microfluidic systems. Wettability control may be accomplished by different activation such as optical, chemical, mechanical and thermal.³ In recent years, zinc oxide (ZnO) films/nanostructures synthesized via different methods have been reported for

reversible light-controlled wetting (hydrophobic/hydrophilic) transition.^{4–8}

Zinc oxide is a promising semiconductor as an optoelectronic material due to its large exciton binding energy (60 meV) and wide band gap (3.37 eV). ZnO nanostructures have gained much attention because of their good piezoelectric properties, high energy-conversion efficiency, optoelectronic properties, photoluminescence enhancement and efficient ultraviolet irradiation. ZnO doping with group II elements (Be, Mg, Ca, Sr, Ba) enhances its optoelectronic and photoluminescence properties by the modification of the grain size and selectivity of the structure. Group II element calcium and magnesium doping in ZnO is well known for band gap engineering and photocatalytic activity.^{9–11} Calcium-doped ZnO thin films have outstanding properties including high piezoelectric coefficient and chemical stability and low acoustic absorption for thin-film transistors, microelectromechanical systems (MEMS) and surface acoustic wave devices.^{12–14} Moreover, Mg- and Ca-doped ZnO nanostructures are widely used for the detection of different gases (ammonia, CO₂, CO, NO₂). Therefore, by successful doping, one can increase the selectivity toward

✉ Faran Baig
faran_baig@yahoo.com

¹ Department of Physics, GC University, Lahore 54000, Pakistan

the target gas by modifying the surface and enhance gas adsorption.^{11,14,15} Mahdhi et al.¹⁶ prepared transparent Ca:ZnO films with visible transmittance (>80%) and a band gap of 3.33 eV for 3 at% Ca by magnetron sputtering. Wang et al.¹⁷ reported a magnesium-doped zinc oxide ($\text{Mg}_{0.2}\text{Zn}_{0.8}\text{O}$) nanostructure used as a detector for UV detection. Khranovskyy et al.¹⁸ prepared ZnO nanostructures by atmospheric pressure metal organic chemical vapor deposition (APMOCVD) and investigated the UV light-induced super-hydrophilicity by the surface chemistry of the ZnO nanostructures. Li et al.¹⁹ prepared ZnO nanoflakes to investigate the water contact angle by UV exposure. Wang et al.²⁰ synthesized ZnO nanoarrays to investigate the wettability of different nanostructures.

Colson et al.²¹ prepared ZnO nanowires by a hydrothermal method and explained the reversible wettability after UV illumination. Chi et al.²² fabricated ZnO films by glancing-angle deposition (GLAD) and explored modification of the wetting state from hydrophobic to hydrophilic by UV light irradiation. Rajesh et al.²³ prepared ZnO nanorods by a hydrothermal method and examined the wettability states by UV irradiation. In our previous study, calcium and magnesium were co-doped using a sol-gel method and we investigated the co-doping effects on the surface wettability (hydrophilic and hydrophobic).²⁴ So far, the effects of Ca and Mg doping on the wetting, UV light-induced wettability and UV sensing performance of ZnO thin films have not been well explored, which is the main objective of this work. Therefore, the effects of calcium and magnesium on ZnO nanostructure shapes were explored, as well as the influence on the ZnO nanostructure with multiple properties, i.e., UV light-induced super-wetting and sensitivity, for sensor applications with super-hydrophilic behavior. The super-hydrophilicity enhances the self-cleaning behavior.

According to the above discussion, in this study, flower-, cotton- and rod-type Ca- and Mg-doped ZnO thin films were prepared by the chemical bath deposition method (CBD) to investigate their optical, UV light-induced wetting properties and UV sensing performance. The variation in different properties was explored by X-ray diffraction spectroscopy (XRD), scanning electron microscopy (SEM), ultraviolet-visible (UV-vis) spectroscopy, contact angle system and UV irradiation.

Experimental

Seed Layer Preparation

Seed layers provide nucleation sites for the growth of nanostructures. The seed layer preparation on the substrate is an important procedure for the homogeneous growth of the nanostructure on the substrate by CBD. Here, the seed

layer was prepared by a sol-gel spin-coating technique on acetone-cleaned glass substrates. Zinc acetate dehydrate ($\text{Zn}(\text{CH}_3\text{COO})_2 \cdot 2\text{H}_2\text{O}$), 2-methoxyethanol and monoethanolamine (MEA) were used as host precursor, solvent and stabilizing agent, respectively. The procedure and all conditions adopted to prepare the ZnO solution, seed layer and CBD procedure were reported in our previous work.²⁵

Calcium-Doped ZnO Thin Films by CBD

Zinc acetate dehydrate (Panreac, Spain), calcium nitrate hexa-hydrate (Duksan, South Korea) and magnesium acetate tetra-hydrate (Sigma-Aldrich, USA) were used as host and dopant reagent. The chemicals were AR, ACS grade and purchased from Ghani Scientific company, Maclagan Road, Lahore, Pakistan. The concentration of dopant varied as $x = 0, 5$ and 10 wt. at%. The dopant/host ratios were $(\text{dopant})_x\text{Zn}_{1-x}\text{O}$. The required quantity of both (precursor and dopant) was dissolved in 125ml of deionized (DI) water for the preparation of 25mM solution. Another solution of 20mM in DI water of hexamine was made. Both prepared solutions were mixed in a beaker (double wall). The seeded substrates (ZnO spin coated film on glass substrate) were dipped vertically in this beaker when CBD equipment temperature touched 85°C and remained at this position for three hours. Finally, all samples were washed with DI water and after drying annealed at 450 °C for two hours. The sample's assigned names were: ZnO (sample 1), 5% CaZnO (sample 2), 10% CaZnO (sample 3), 5% MgZnO (sample 4) (reported in previous work),²⁵ 10% MgZnO (sample 5). Figure 1

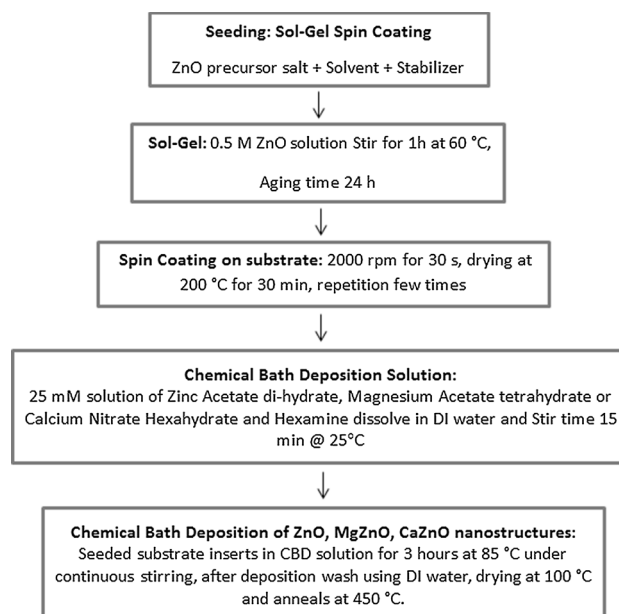


Fig. 1 Flow chart for the synthesis of ZnO, MgZnO and CaZnO nanostructures

shows the general procedure flow diagram for the preparation of ZnO and doped ZnO films from seeding to CBD.

The crystal structures were analyzed by X-ray powder diffractometer (PANalytical PW 3040/60 X'Pert Pro) with Cu K α ($k = 1.5406 \text{ \AA}$). The surface morphology was observed by scanning electron microscopy (SEM) (JEOL JSM-6480LV) with 10K magnification, and EDS (JEOL JEE-420 coupled with SEM) was used for elemental analysis. For optical measurement, a UV-vis spectrophotometer (Ocean Optics USB4000) was used in the wavelength range of 350–800nm. The contact angle measurement was recorded by a self-designed measuring system. The photo-induced super-hydrophilic behavior and sensing performance was observed by UV lamp Spectronics PE-24 T/F of wavelength 254nm with UV index 4.

Results and Discussion

(i) XRD Analysis:

XRD characterization provides information about the structure of the material.²⁶ Figure 2 depicts the X-ray diffraction spectra of ZnO, CaZnO and 10% MgZnO films prepared by chemical bath deposition and recorded in the range of 20–80°. However, 5% MgZnO XRD spectra using 2-methoxyethanol solvent was reported previously (solvent study),²⁵ which revealed the most dominant sharp peak of (002) plane. Figure 2a shows the ZnO spectrum and reveals the polycrystalline nature with dominant c-axis (perpendicular to the substrate) morphology by the highest peak of (002). The dominant (002) peak ascribed to the majority of ZnO nanostructure growth morphology was perpendicular to the substrate surface. Figure 2b presents the CaZnO results revealing multi-orientation morphology with a dominant orientation along the a-axis (101) plane (parallel to the substrate).²⁷ Likewise, Fig. 2c shows the 10% MgZnO spectrum and reveals dominant c-axis (perpendicular to the substrate) morphology via the highest peak of the (002) plane. Furthermore, the FWHM is clearly broader for the CaZnO samples than the ZnO and MgZnO samples, which had narrower FWHM. The narrow FWHM is obviously attributable to the larger grain size for ZnO, whereas the broader FWHM confirms the smaller grains for the CaZnO samples.²⁸ This also suggested that the crystallinity of CaZnO film deteriorated.

(ii) SEM and EDS Analysis:

SEM images for sample 1 (ZnO), sample 2 (5% Ca content in ZnO), sample 3 (10% Ca content in ZnO) and sample 5 (10% Mg content in ZnO) shown in Fig. 3. However, sample 4 (5% Mg content in ZnO) reported previously²⁵ and depicted closely oriented nanorods perpendicular to the substrate. Rod-, flower- and cotton-type structure found

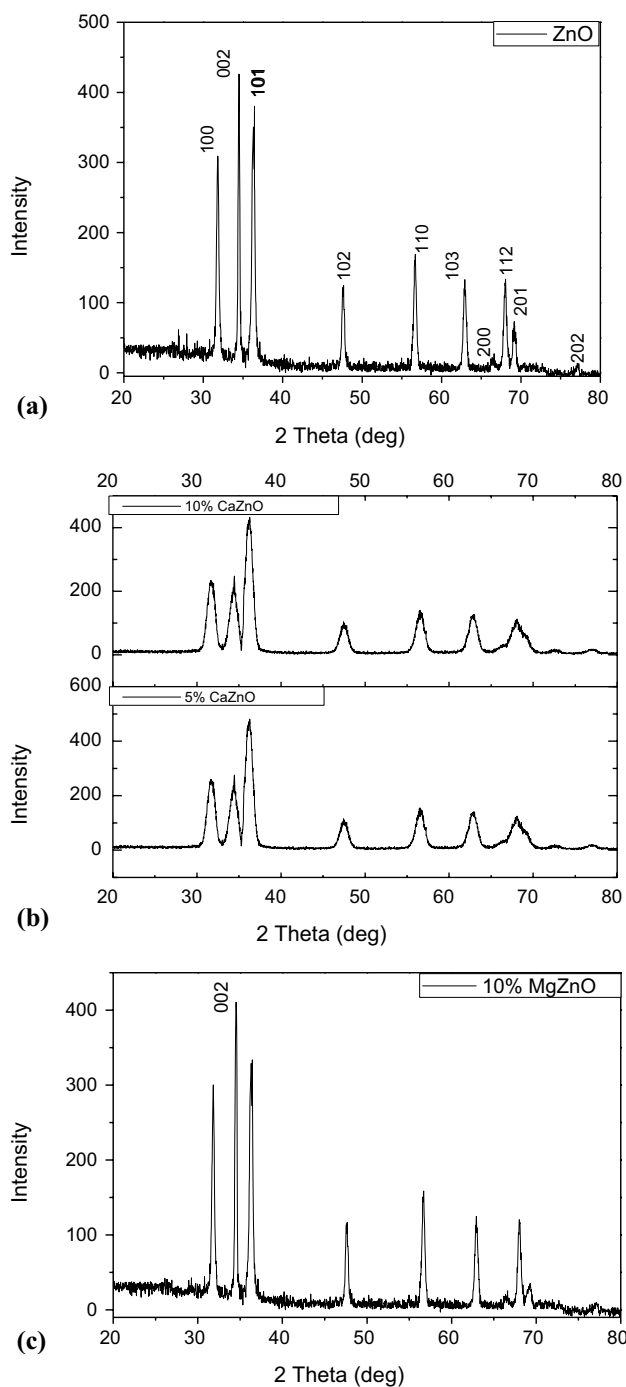


Fig. 2 XRD plots for (a) ZnO; (b) 5% Ca-doped ZnO, 10% Ca-doped ZnO; and (c) 10% Mg-doped ZnO

for the sample 1, sample 5, sample 2 and sample 3, respectively. Sample 2 presented dense nanoflowers, however as the doping concentration increased from 5% to 10% (sample 3) the structure of sample converted to cotton-like structure. The SEM and XRD plot of ZnO seed layer using 2-methoxyethanol solvent was presented in our previous work.²⁵ The previous study focused on seed layer solvent effects on

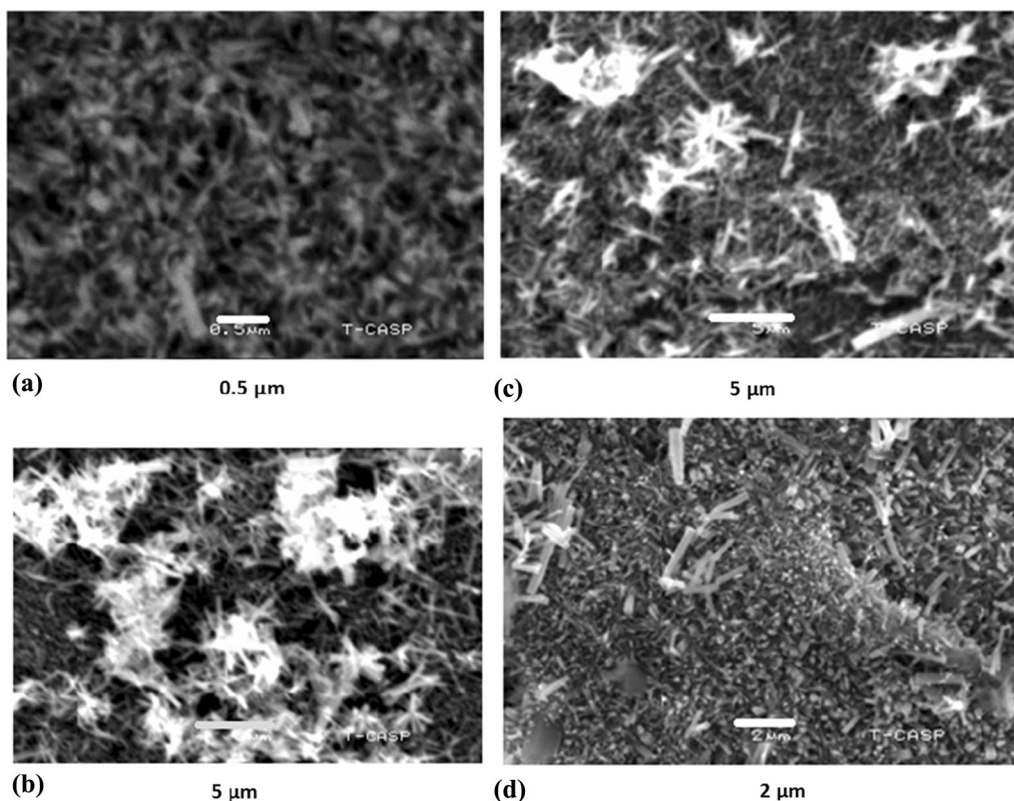


Fig. 3 SEM images: (a) ZnO, (b) 5% Ca-doped ZnO, (c) 10% Ca-doped ZnO and (d) 10% Mg-doped ZnO

5% Mg-doped ZnO nanostructures. The preparation of the seed layer before the chemical bath process is important for homogeneous and well-aligned growth of the nanostructure. The seed layer delivered nucleation sites for the evolution and initiative growth of ZnO, CaZnO and MgZnO nanostructures during the chemical bath process. Interestingly, the dominant growth of ZnO and MgZnO nanorods (sample 1, sample 4 and sample 5) along the c-axis, as revealed by XRD, may be attributed to the homogeneous growth of the nanorods on the c-axis-oriented seed layer. On the other hand, calcium-doped samples (sample 2 and sample 3) produced multi-orientation (dominated a-axis) (flower and cotton), attributed to non-homogeneous growth morphology due to the difference in the ionic radius of Zn and Ca. Conversely, both Zn and Mg have comparable ionic radii.

EDS characterization is necessary to evaluate the presence of elements in the material. Figure 4 presents the EDS spectra and weight percent table for sample 2 and sample 3 (CaZnO) whereas MgZnO was reported in our previous work.²⁵ Figure 4 shows peak at 1.01 KeV, which clearly indicates the presence of zinc. The peak at about 0.52 KeV suggested the presence of oxygen. Likewise, the intensity of a peak near 3.81 KeV confirmed the presence of calcium in the zinc oxide film samples. The result in Table I shows the percentage of each element present in the samples. It

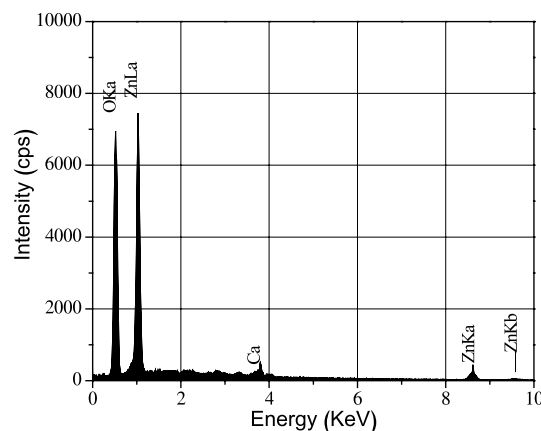


Fig. 4 Ca-doped ZnO EDS spectra

elucidates clearly that the weight percentage of calcium improved from 2.82 to 4.43 as the calcium concentration increased from 5% to 10 at% in the deposited ZnO nano films.

(iii) Optical Analysis:

The plots of transmittance and band gap for all samples are shown in Fig. 5. The measured optical transmittance lies

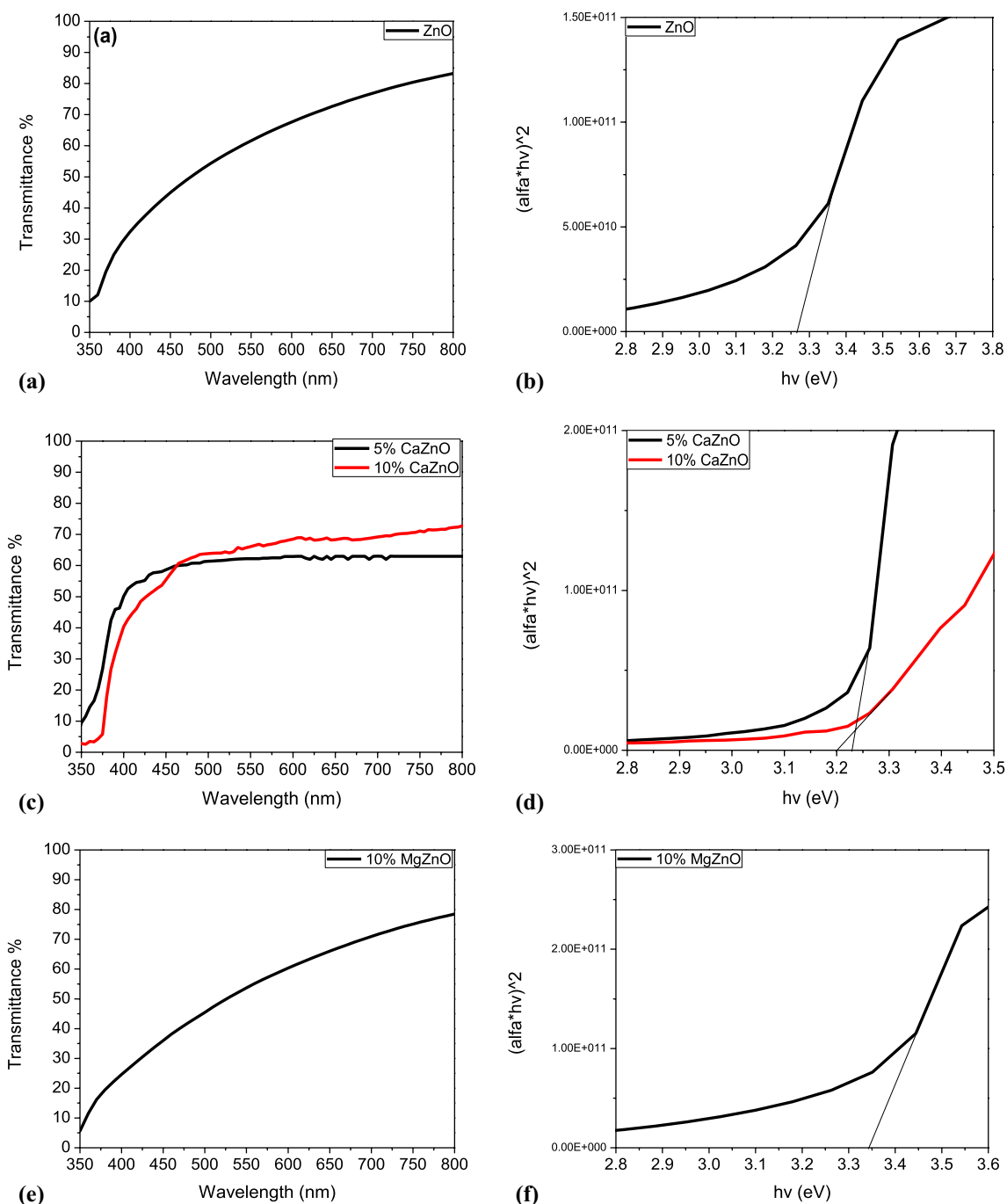


Fig. 5 UV-vis plots for (a) ZnO transmittance, (b) ZnO band gap, (c) 5% and 10% Ca-doped ZnO transmittance, (d) 5% and 10% Ca-doped ZnO band gap, (e) 10% Mg-doped ZnO transmittance and (f) 10% Mg-doped ZnO band gap

between 350 and 800 nm. Information from transmittance plots clearly explained a good percentage of transmittance produced by all the samples because of the better quality of the films.²⁹ The maximum transmittance achieved by sample 1, sample 2, sample 3, sample 4 and sample 5 was 80%, 60%, 70%, 90% and 78%, respectively. The optical results for sample 4 were reported previously.²⁵ Oscillations in the

transmittance spectra were produced by the interference in the films. As the Ca doping increased from 5% to 10 at% for sample 2 and 3, the transmittance decreased as presented in Fig. 5c due to the substitution of more foreign atoms in Zn lattice and structural change (random alignment of structure). However, in case of MgZnO samples, the transmittance increased and remains nearly unchanged due to the

better alignment of nanorods in the c-axis direction. A clear shift of transmittance to higher wavelength confirmed the Ca incorporation in ZnO. Also, the obvious red shift occurred may be because of the larger ionic radius of Ca than Zn. Likewise, the blue shift occurred with Mg doping by the decrement of wavelength. The absorption coefficient (α) was calculated through the absorbance (A) data and film thickness (t) using the following relation.³⁰

$$\alpha = 2.303 \left(\frac{A}{t} \right) \quad (1)$$

The calculation of band gap was performed using Tauc's equation.^{25,31}

$$\alpha(h\nu) = B(h\nu - E_g)^n \quad (2)$$

Here ($h\nu$) is called as photon energy and α is the absorption coefficient. The terms B and E_g are the constant and optical energy gap, respectively. It is known that ZnO is a direct band gap system, and hence the $\alpha(h\nu)^2$ and ($h\nu$) plot should provide linear behavior which is related to the strong absorption in the absorption edge. Therefore, the take-up of the linear portion with $\alpha = 0$ provides the optical energy gap. The Tauc plot in Fig. 5b, d and f shows the band gap of samples 1 to 5 as 3.26 eV, 3.23 eV, 3.20 eV, 3.3 eV (reported previously²⁵) and 3.34 eV, respectively. The band gap increased by Mg doping was due to the Moss-Burstein effect³². However, the decreased band gap by Ca doping may be attributed to the presence of defects by the higher ionic radius of Ca than Zn.³³

(iv) Wettability Analysis:

The processes of wettability are surface-facilitated, and surface topography is the main factor governing the wettability of the surface. The wettability of the ZnO, CaZnO and MgZnO nanostructures was measured via static contact angle (CA) as displayed in Fig. 6. The ZnO structure presented a strong hydrophobic surface, with a water contact angle of 135°. The calcium-doped ZnO samples demonstrated both hydrophobic and hydrophilic behavior, with contact angles of 90° and 85°. Similarly, the magnesium-doped ZnO samples demonstrated super-hydrophobic and strong hydrophobic behavior, with contact angles of 152° and 140°. The CA values are plotted in Figs. 7a and 8a with doping increment.

The wettability on the zinc oxide structure can be considered by the Wenzel or Cassie-Baxter models.^{34,35} For a drop of liquid on the surface, the contact angle is determined by the surface free energies involved.³⁶

$$\cos \theta = (\gamma_{sv} - \gamma_{sl})/\gamma_{lv} \quad (3)$$

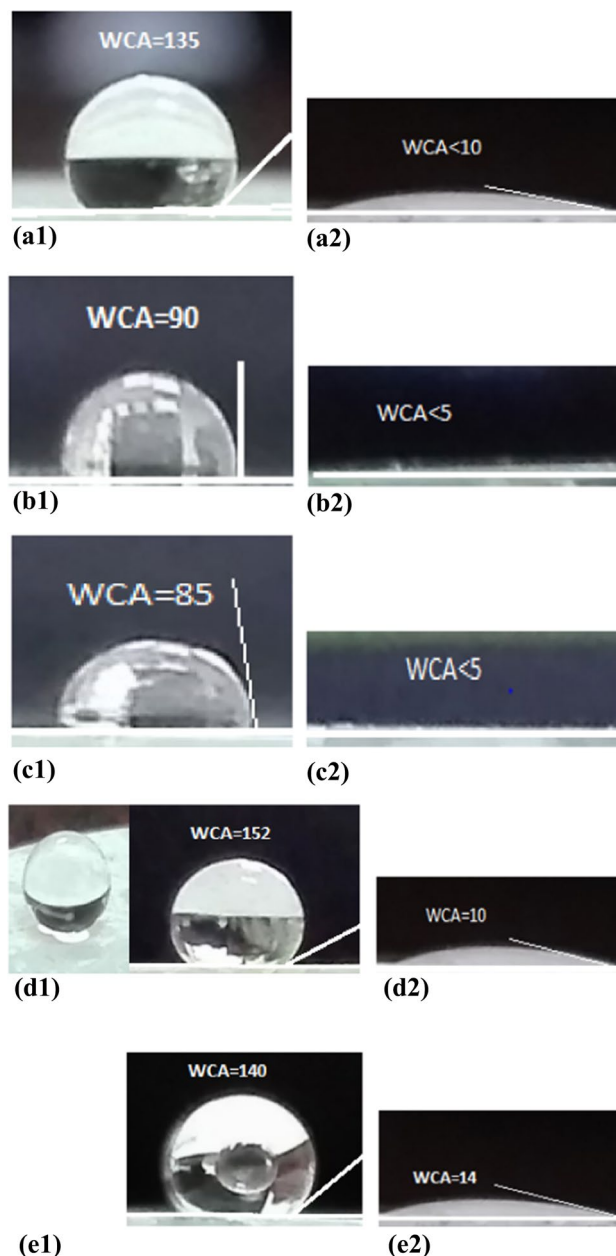


Fig. 6 Water contact angle before (a1) ZnO, (b1) 5% CaZnO, (c1) 10% CaZnO, (d1) 5% MgZnO with upper side image, (e1) 10% MgZnO nanostructures, and after 2 h (a2) ZnO, (b2) 5% CaZnO, (c2) 10% CaZnO, (d2) 5% MgZnO, (e2) 10% MgZnO nanostructures, UV irradiation

where γ_{sv} , γ_{sl} , and γ_{lv} are the solid/vapor, solid/liquid, and liquid/vapor tensions, respectively.

In order to observe the wetting states of all ZnO, CaZnO and MgZnO nanostructures, UV light (wavelength 254 nm) irradiation was carried out, which provided photon energy greater than the zinc oxide band gap energy. The time of UV irradiation varied from 0 to 2 h, and the wettability for each sample was measured every 40 min, as presented in the

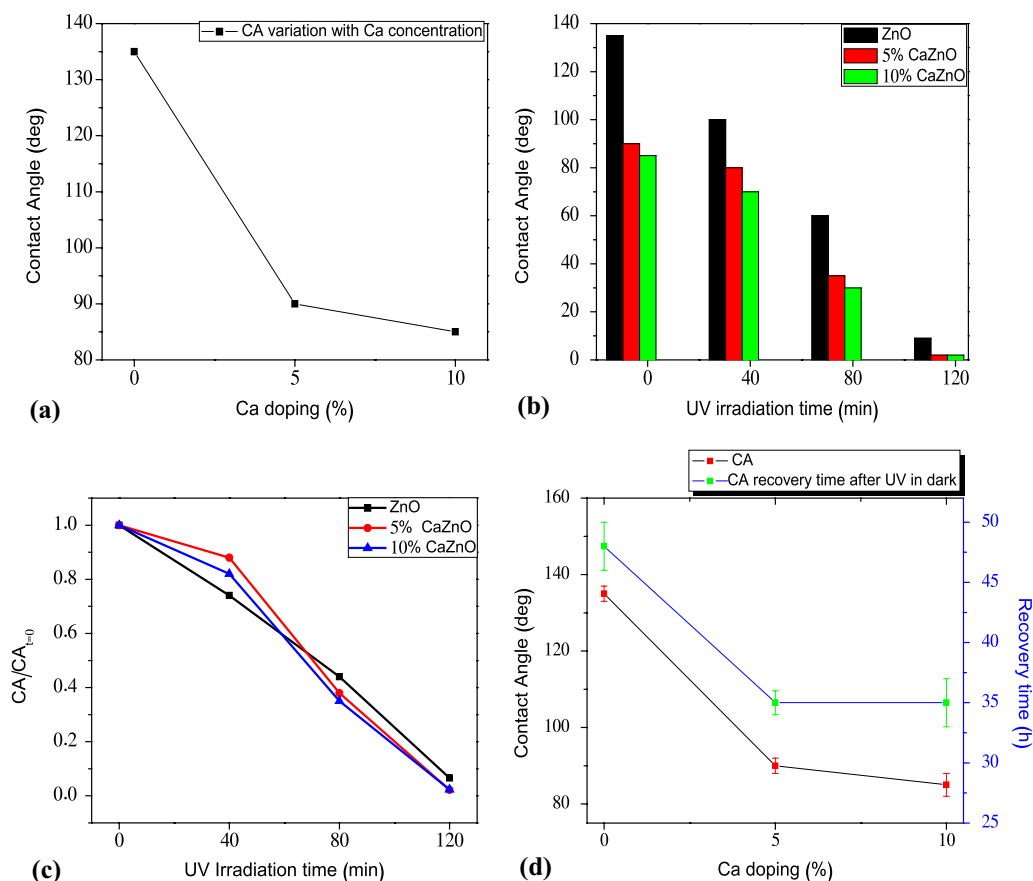


Fig. 7 Plots for (a) WCA variation with Ca concentration, (b) CA reduction with UV irradiation, (c) CA reduction rate, and (d) CA recovery with time plot

plots of Figs. 7b and 8b. After the irradiation on all the samples, a change in the wettability state from hydrophobic to hydrophilic was observed. This change was attributed to the zinc oxide and calcium- and magnesium-doped zinc oxide semiconductor nature. Similar results have been reported in the literature for TiO_2 .^{37,38}

When ultraviolet light with photon energy greater than the ZnO, CaZnO and MgZnO band gap was allowed to fall on the samples, a significant number of valence electrons were excited to the conduction band, leaving behind the same number of holes in the valence band. A few of these holes reacted with lattice oxygen, whereas the excited electrons reacted with the Zn lattice to form surface oxygen vacancies and Zn defect sites, respectively. Therefore, water and oxygen may adsorb on these defective sites. This resulted in more adsorption of water on the irradiated area of the sample. As a consequence, the hydrophilic behavior greatly improved to super-hydrophilic and WCA decreased for the ZnO, CaZnO and MgZnO surface.³⁷

This wettability change mechanism was applicable to all the samples of ZnO, CaZnO and MgZnO nanostructures. It is worth mentioning that the arrangement and shape of the

nanostructure samples play a major role in the perceived effect. During UV exposure, the wettability change was the transformation of states (Cassie-Baxter to Wenzel). In the Wenzel state, the water droplet is completely fixed on the solid surface, whereas in the Cassie-Baxter state it is not fixed or completely touching the surface. Therefore, after UV irradiation, the water droplet began to penetrate the nanostructure surface. Moreover, the surface energy was increased by the irradiation, and water penetration reduced the surface roughness. Together, these mechanisms helped to produce the super-hydrophilicity of the sample surfaces. Hence, after a certain time period all the samples demonstrated super-hydrophilic performance.

The time for the transition from the hydrophobic or super-hydrophobic to the super-hydrophilic state was greatly dependent on the surface morphology. The most rapid variation in CA (hydrophobic to super-hydrophilic) was found for the CaZnO samples. The decrease in the contact angle was due to the photocatalytic reaction on the sample surface.

The relative changes in contact angle (wettability transition) were determined, and the normalized CA evolution is presented in Figs. 7c and 8c. The CA reduction rate was

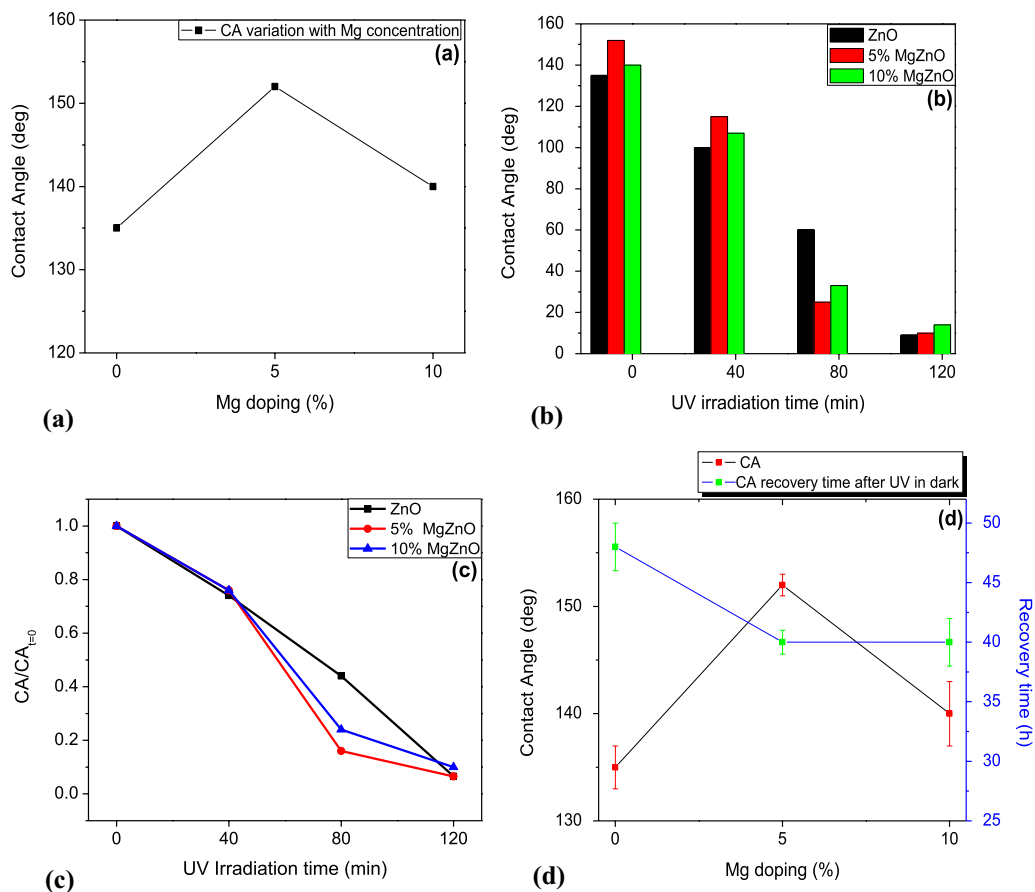


Fig. 8 Plots for (a) WCA variation with Mg concentration, (b) CA reduction with UV irradiation, (c) CA reduction rate, and (d) CA recovery with time plot

Table I Weight percent table

Element	Wt.% (5% CaZnO)	Wt.% (10% CaZnO)
O	44.13	42.06
Ca	2.82	4.43
Zn	53.05	53.51

estimated by dividing each contact angle (after UV irradiation) value to CA at $t = 0$. The reduction rate is an efficiency measure of the light-induced process. The value of the normalized reduction rate, after 120 min of exposure, was found to be lower for the CaZnO nanostructures of samples 2 and 3, i.e., 0.022 and 0.023, respectively, compared to the ZnO and the 5% and 10% MgZnO samples, i.e., 0.066, 0.065 and 0.1, respectively. It should be noted that the normalized value of CA after exposure for 40 min was lower for ZnO than for CaZnO, which may be attributed to the higher surface energy produced by UV light. Subsequently, due to the dominant structural chemistry (nanorod), the normalized value of the reduction rate for ZnO was higher. Likewise, its

value decreased significantly for MgZnO samples, which can also be attributed to the higher surface energy produced by the UV light. Figures 7d and 8d present the recovery status of the contact angle by the storage of all samples in the dark. During dark storage, the absorbed electrons and holes (to form hydroxyl groups) are replaced by oxygen atoms. Therefore, the surface reverted back to its initial state, and the wetting state reconverted from super-hydrophilic to strong and super-hydrophobic states. The recovery times for CaZnO and MgZnO samples were approximately 35 and 40 h, respectively. The greater light-induced wettability observed for the CaZnO sample can be attributed to the water insertion in its flower- and cotton-type structures, which made their surface less rough. However, lesser wettability in ZnO and MgZnO samples may be attributed to their well-aligned nanorod structure.

(v) UV Sensitivity:

The UV response measurements were performed using a customized circuit exploiting the built-in capabilities of modern microcontrollers (μC). Modern microcontrollers

are typically equipped with built-in analog-to-digital (ADC) conversion facility. In this case, Arduino Uno was used to measure the variation in the sample resistance. The samples were made to constitute one segment of a voltage divider circuit. Due to the very high nominal resistance of the samples and the resolution limit of the microcontroller, a 1 M Ω resistance was used to complete the voltage divider circuit. The input voltage was DC 5V. The sample was used as a sensor in a metal-semiconductor-metal (MSM) configuration and was kept under the UV lamp box. The wavelength of the UV lamp used in all experiments was 254 nm. Generally, molecules of oxygen may adsorb on a sample surface when exposed to ambient air. These oxygen molecules trap electrons from the sample, which generates negatively charged ions on the sample surface. Therefore, a depletion layer is formed, which decreases the sample conductivity. On the contrary, under UV illumination, electron-hole pairs are generated with photon energy higher than the band gap energy. These holes recombine with the negatively charged ions. Consequently, the conductivity of the sample recovers by the unpaired electrons that make the depletion layer thin.

Figure 9a shows a comparative plot for all the samples as a switching characteristic of UV sensors with the modulation of UV light with a time interval of 60 s. When the UV light turned on, the photo-response (voltage) decreased rapidly due to the reduction in sample resistance by the photo-generated electrons, and when it was switched off, the photo-response increased dramatically. This revealed the good strength and reproducibility of the samples as a UV sensor. It can be noted that the voltage response for the 5% Mg-doped ZnO sample was faster and larger than that of the other samples, as plotted in Fig. 9b. This may be attributed to the better crystallinity and *c*-axis orientation of the nanorods, as revealed by XRD and SEM results, and better electron transport. This also indicates the transparent (compared to other samples) photo-sensor as revealed by transmittance of 90%, extraordinarily suitable for fast switching UV operation, i.e., response and recovery. The better photo-response shown for this sample compared to the others when the UV illumination was on and off was because oxygen desorption and adsorption near the sample surface happened rapidly.³⁹ On the other hand, the calcium-doped samples produced low UV response, as a noisy signal due to low crystallinity and randomly oriented nanostructure (flower and cotton) produced a potential barrier in the electron path and resulted in electron transport delay, which in turn degraded the photo-sensitivity of these samples.⁴⁰ Table II shows the response and recovery time for the Mg-doped samples compared with the literature.

Table II Characteristic values for ZnO sensors

Sample	Response time (s)	Recovery time (s)
ZnO	55	60
5% MgZnO	45	50
10% MgZnO	48	55
Porous ZnO ⁴¹	250	150
Ga-doped ZnO ⁴²	95	2068
ZnO micro-flowers ⁴³	85.18	112.9
ZnO nano network ⁴⁴	15	330
20% MgZnO Nanorods ⁴⁵	24.5	18.4

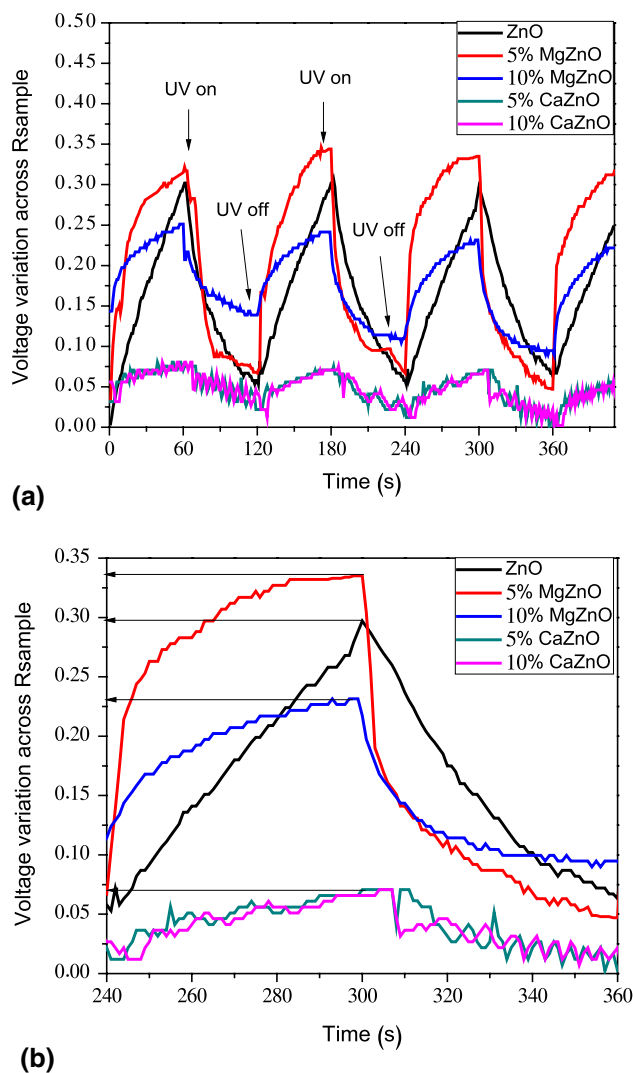


Fig. 9 (a) Comparative time-dependent photo-response (voltage) of the ZnO, MgZnO and CaZnO samples; (b) voltage comparison among all samples for one cycle.

Conclusions

The calcium-doped ZnO (CaZnO) and magnesium-doped ZnO (MgZnO) nanostructures were well synthesized on glass substrates by chemical bath deposition. Various properties of the CaZnO and MgZnO films (0, 5 and 10 at.% Ca, Mg-doped ZnO) were investigated. The XRD results show (002) plane dominant morphology for the ZnO and MgZnO nanorods and (101) plane dominance for the CaZnO nanostructures. The SEM results showed more cotton-type structure for the 10% Ca concentration and c-axis-oriented nanorods for 5% Mg concentration. The transmittance was found to be above 80%, 60% and 70% for 0–10% CaZnO films and 90% and 78% for 5–10% MgZnO films, respectively. The band gaps explored were 3.26 eV, 3.23 eV and 3.20 eV for 0–10% CaZnO films; and 3.3 eV and 3.34 eV for 5–10% MgZnO films, respectively. The water contact angles (WCA) for the 5% Ca and Mg concentrated samples were 90° and 152°, respectively. Super-hydrophilicity was observed for all samples by UV light irradiation. The value of the reduction rate of the contact angle was as low as 0.022 and 0.065 for the calcium- and magnesium-doped nanostructures, respectively. Moreover, the lowest CA recovery time of around 35 h was found for the CaZnO films. The UV sensing performance was evaluated for all the samples, and the best rise-fall time (45–50s) with photo-response (voltage = 0.35V) was found for the 5% Mg-doped ZnO sample. Therefore, magnesium doping for ZnO nanostructures is suitable for UV sensing applications with less wettability and super-hydrophobic properties.

Acknowledgments The authors would like to thank the Department of Physics, GC University Lahore.

Declarations

Conflict of interest The authors declare that they have no conflict of interest

References

- E.S. Ates, S. Kucukyildiz, and H.E. Unalan, *Appl. Mater. Interf.* 4, 5142 (2012).
- P.-N. Ni, C.X. Shan, S.P. Wang, B.H. Li, Z.Z. Zhang, D.X. Zhao, L. Liu, and D.Z. Shen, *J. Phys. Chem. C* 116, 1350 (2012).
- N. Verplanck, Y. Coffinier, W. Thomy, and R. Boukherroub, *Nanoscale Res. Lett.* 2, 577 (2007).
- E. Velayi, and R. Norouzbeigi, *Surf. Coat. Technol.* 367, 252 (2019).
- V. Kekkonen, A. Hakola, T. Kajava, E. Sahramo, J. Malm, M. Karppinen, and R.H.A. Ras, *Appl. Phys. Lett.* 97, 044102 (2010).
- G. He, S. Lu, W. Xu, P. Ye, G. Liu, H. Wang, and T. Dai, *J. Alloy Compd.* 747, 772 (2018).
- J. Lu, K. Huang, X. Chen, J. Zhu, F. Meng, X. Song, and Z. Sun, *Appl. Surf. Sci.* 256, 4720 (2010).
- N. Tarwal, and P.S. Patil, *Appl. Surf. Sci.* 256, 7451 (2010).
- A. Irshada, A. Ejaz, M. Ahmad, M.S. Akhtar, M.A. Basharat, W.Q. Khan, M.I. Ghauri, A. Ali, and M.F. Manzoor, *Mater. Sci. Semicond. Process.* 105, 104748 (2020).
- R. Slama, J.EI. Ghoul, K. Omri, A. Houas, L.EI. Mir, and F. Lounay, *J Mater Sci: Mater Electron* 27, 7939 (2016).
- A.J. Kulandaisamy, J.R. Reddy, P. Srinivasan, K.J. Babu, G.K. Mani, P. Shankar, and J.B.B. Rayappan, *J. Alloys Compd* 688, 422 (2016).
- W. Yu, D. Han, G. Cui, Y. Cong, J. Dong, X. Zhang, X. Zhang, Y. Wang, and S. Zhang, *Jpn. J. Appl. Phys.* 55, 1 (2016).
- L.L.P. Wong, S. Na, A.I. Chen, Z. Li, M. Macecek, and J.T.W. Yeow, *Sens. Actuat. A-Phys.* 247, 430 (2016).
- A. Ghosh, C. Zhang, S. Shi, and H. Zhang, *Sens. Actuat. B Chem.* 301, 126958 (2019).
- R. Dhahri, S.G. Leonardi, M. Hjiri, L. El Mir, A. Bonavita, N. Donato, D. Iannazzo, and G. Neri, *Sens. Actuat. B* 239, 36 (2017).
- H.Z.K. MahdhiBen AyadiDjessas, *J. Solid State Electrochem.* 23, 3217 (2019).
- H. Wang, Q. Liu, X. Wang, He. Tang, J. Yan, and P. Gao, *J. Mater. Sci.: Mater. Electron.* 31, 505 (2020).
- V. Khranovskyy, T. Ekblad, R. Yakimova, and L. Hultman, *Appl. Surf. Sci.* 258, 8146 (2012).
- H. Li, H. Lu, S. Liu, Q. Li, and Q. Liu, *Mater. Res. Bull.* 114, 85 (2019).
- J. Wang, B. Weng, P. Larson, and Y. Liu, *Surf. Interfaces* 16, 188 (2019).
- P. Colson, A. Schrijnemakers, B. Vertruyen, C. Henrist, and R. Cloots, *J. Mater. Chem.* 22, 17086 (2012).
- P.-W. Chi, Su. Chih-Wei, and D.-H. Wei, *Appl. Surf. Sci.* 404, 380 (2017).
- Y. Rajesh, D.D. Purkayastha, and M. G. Krishna, *J. Alloys and Compounds*, 157617 (2020).
- F. Baig, A. Asif, M.W. Ashraf, and H.M. Fahad, *J. Sol-Gel. Sci. Technol.* 97, 706 (2021).
- F. Baig, A. Asif, M.W. Ashraf, and M. Imran, *Mater. Res. Express* 7, 026417 (2020).
- A.S. Hassanien and U.T. Khatoon, *Physica B* 554, 21 (2019).
- D. Aryanto, P. Marwoto, T. Sudiro, A. S. Wismogroho, and Sugianto, *IOP Conf. Ser. J. Phys. Conf. Ser.* 1191, 012031 (2019).
- A.S. Hassanien, A. A. Akl, A.H. Sáaedi, *CrystEngComm* 20, 1716 (2018).
- A.S.I.A..A. HassanienSharmaAkl, *J. Non-Cryst. Solids* 531, 119853 (2020).
- M. Shkir, M. Arif, V. Ganesh, M.A. Manthrammel, I.S. Arun Singh, Y. Shivaraj, R. Maidur, P.S. Patil, and S. AlFaify, *J. Mol. Struct.* 1173, 375 (2018).
- A.S. Hassanien, and I.M. El Radaf, *Phys. B Phys. Condens. Matter* 585, 412110 (2020).
- P. Fermi Hilbert Inbaraj, and J. Joseph Prince, *J Mater Sci: Mater Electron* 29, 935 (2018).
- A.-I. Istrate, F. Nastase, I. Mihalache, F. Comanescu, R. Gavriila, O. Tutunaru, C. Romanitan, V. Tucureanu, M. Nedelcu, and R. Müller, *J. Sol-Gel. Sci. Technol.* 92, 585 (2019).
- R.N. Wenzel, *Ind. Eng. Chem.* 28, 988 (1936).
- A.B.D. Cassie, and S. Baxter, *Trans. Faraday Soc.* 40, 546 (1944).
- T. Young, *Philos. Trans. R. Soc. London* 95, 65 (1805).
- R.D. Sun, A. Nakajima, A. Fujishima, T. Watanabe, and K. Hashimoto, *J. Phys. Chem. B* 105, 1984 (2011).
- M. Miyauchi, N. Kieda, S. Hishita, T. Mitsuhashi, A. Nakajima, T. Watanabe, and K. Hashimoto, *Surf. Sci.* 511, 401 (2002).
- C. Soci, A. Zhang, B. Xiang, S.A. Dayeh, D.P.R. Aplin, J. Park, X.Y. Bao, Y.H. Lo, and D. Wang, *Nano Lett.* 7, 1003 (2007).
- J.T.A.I.M.S.R.V. AgrawalDixitPalaniRaoSingh, *Phys. Status Solidi RRL* 12, 1800241 (2018).

41. N. Nasiri, R. Bo, F. Wang, L. Fu, and A. Tricoli, *Adv. Mater.* 27, 4336 (2015).
42. L. Mandalapu, F. Xiu, Z. Yang, and J. Liu, *Solid-State Electron.* 51, 1014 (2007).
43. M.A. Khan, M.K. Singha, K.K. Nanda, and S.B. Krupanidhi, *Appl. Surf. Sci.* 505, 144365 (2020).
44. X. Wang, K. Liu, X. Chen, B. Li, M. Jiang, Z. Zhang, H. Zhao, D. Shen *A.C.S. Appl. Mater. Interf.* 9, 5574 (2017).
45. Y. H. Liu, S-J. Young, C. H. Hsiao, L-W. Ji, T. H. Meen, W. Water, and S-J. Chang, *IEEE Photon. Technol. Lett.*, 26 (7), (2014).

Publisher's Note Springer Nature remains neutral with regard to jurisdictional claims in published maps and institutional affiliations.